

Title	Pulse cluster dynamics in passively mode-locked semiconductor vertical-external-cavity surface-emitting lasers
Authors	Hausen, Jan;Meinecke, Stefan;Lingnau, Benjamin;Lüdge, Kathy
Publication date	2019-04-17
Original Citation	Hausen, J., Meinecke, S., Lingnau, B. and Lüdge, K. (2019) 'Pulse cluster dynamics in passively mode-locked semiconductor vertical-external-cavity surface-emitting lasers', <i>Physical Review Applied</i> , 11(4), 044055 (13pp). doi: 10.1103/ PhysRevApplied.11.044055
Type of publication	Article (peer-reviewed)
Link to publisher's version	<a href="https://link.aps.org/doi/10.1103/PhysRevApplied.11.044055">https://link.aps.org/doi/10.1103/PhysRevApplied.11.044055</a> - <a href="https://link.aps.org/doi/10.1103/PhysRevApplied.11.044055">10.1103/PhysRevApplied.11.044055</a>
Rights	© 2019, American Physical Society. All rights reserved.
Download date	2024-05-06 23:44:57
Item downloaded from	<a href="https://hdl.handle.net/10468/7995">https://hdl.handle.net/10468/7995</a>



# Pulse Cluster Dynamics in Passively Mode-Locked Semiconductor Vertical-External-Cavity Surface-Emitting Lasers

Jan Hausen,<sup>1,\*</sup> Stefan Meinecke,<sup>1</sup> Benjamin Lingnau,<sup>1,2</sup> and Kathy Lüdge<sup>1</sup>

<sup>1</sup>*Institut für Theoretische Physik, Technische Universität Berlin, Hardenbergstraße 36, Berlin 10623, Germany*

<sup>2</sup>*Physics Department, University College Cork, College Rd, Cork, Ireland*

(Received 23 December 2018; revised manuscript received 26 February 2019; published 17 April 2019)

In recent years different setups based on external cavities have been developed, in order to enhance the performance of pulsed semiconductor mode-locked lasers, namely the peak power and width of the emitted pulses. Depending on the operating conditions and the cavity configuration, pulse cluster solutions emerge with a nonidentical temporal interpulse spacing, which limit the performance of such devices. In this work we present a system of multidelay differential equations to describe the dynamics of a passively mode-locked vertical-external-cavity surface-emitting laser with V-shaped cavity geometry, that allows for an effective modeling and detailed studies of parameter dependencies. We apply numeric integration as well as path-continuation methods to understand the underlying bifurcation scenarios and hence the parameter regions of stable operation. Our investigations indicate that pulse cluster solutions emerge along the fundamental periodic solution branch with a critical influence of the cavity round-trip time on the number of pulses in the cluster. We find regions of multistability of higher-order pulse clusters and predict how different types of dynamics can be favored by tuning the cavity geometry.

DOI: 10.1103/PhysRevApplied.11.044055

## I. INTRODUCTION

As mode-locked semiconductor lasers offer an efficient option to generate periodic short optical pulses, they qualify for diverse applications such as frequency comb generation [1,2] in optical metrology [3] and spectroscopy [4,5] or optical communication [6–8]. Hence, extensive research has been performed in the last decades, with the strive to understand and enhance the performance figures of such devices [6,8–13]. In order to overcome performance limitations of edge-emitting mode-locked semiconductor lasers in comparison to Ti-Sa or solid-state lasers, vertical-external-cavity surface-emitting lasers (VECSELs) have been developed [14,15]. These provide high peak powers in the kW range with pulse durations down to 100 fs at GHz repetition rates [16–18]. One class of mode-locked VECSELs is configured in a way that the gain chip is positioned in between a semiconductor saturable absorber mirror (SESAM) and the out-coupling facet in a V-shaped geometry. Induced by the interaction of the active components via the electric field, tuning the cavity configuration leads to diverse dynamical regions, such as fundamental mode locking (FML), higher harmonic mode locking (HML) and pulse cluster dynamics (PC) [19–23]. The latter are characterized by pulses of the same amplitude with temporal interpulse spacing much smaller

than the fundamental period at which they occur. These pulse cluster dynamics have been reported to limit the peak power and hinder potential applications of mode-locked VECSELs [19]. In order to model these lasers, different approaches were investigated in recent publications. Microscopic models are introduced in Refs. [24–26], which include the influence of microscopic polarization and therefore are suitable to describe the loss conditions on the very-short pulse generation (100 fs). However, their major drawback lies within the high computational cost, which makes them undesirable for large parameter scans. Furthermore, an approach to model the formation of carrier gratings induced by colliding pulses at the absorber is described in Ref. [22]. Adiabatically eliminating microscopic polarization effects in a delay algebraic equation (DAE) model, describing the VECSEL by two-coupled microcavities, is derived in Ref. [27]. This set of DAEs includes microcavity effects and therefore models the complex interplay between filtering and nonlinearity inside the active sections. Nevertheless, the DAE structure imposes the introduction of additional artificial timescales and takes the limit of infinitely fast timescales to reproduce the DAE structure, which renders an extended bifurcation analysis very “challenging.” Moreover, delay differential equations (DDEs) were derived to model a vast range of dynamics in mode-locked VECSELs such as localized states [28–31], however these do not include the distinct features of the external cavity. In this work we present a system of delay

\*hausen@campus.tu-berlin.de

differential equations also accounting for the influences of the V-shaped cavity geometry, namely the backwards traveling pulse. The model is simple enough to apply conventional path continuation methods and therefore conduct a bifurcation analysis of the pulse cluster dynamics in a mode-locked VECSEL. Our results can help to further improve the operation of such devices, as we reveal multistabilities between different pulse cluster solutions and further unwanted dynamical regions. Furthermore, we also show how higher-order pulse-cluster emission dynamics can be favored by tuning the cavity geometry.

The paper is structured in the following sections: We start by introducing the system of delay differential equations used to model the pulse cluster dynamics found in VECSELs in Sec. II. A bifurcation analysis of the emerging pulse clusters containing a different number of pulses is presented in the results, Sec. III. We describe the generation mechanism of pulse clusters in Sec. III A. A numerical analysis unraveling the emergence of higher-order pulse clusters at increased cavity round-trip times is presented in Sec. III B. In this section we also assess how the pulse clusters stabilize (Sec. III B 1) and how they become independent of the fundamental main solution branch (Sec. III B 2). Additionally, we discuss the effects of introducing a slight asymmetry in the cavity geometry in Sec. III C. A conclusion is given in Sec. IV.

## II. MODEL

In order to account for the distinct features of the V-shaped cavity geometry (see Fig. 1), we derive a DDE-model starting from the traveling wave equations [32]. As the timescales important for the generation of pulse cluster dynamics are much slower than the timescales of

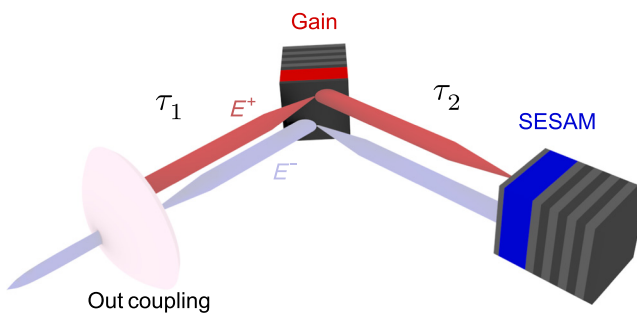


FIG. 1. Sketch of a passively mode-locked VECSEL with V-shaped cavity geometry and symmetric positioning of gain and absorber, i.e.,  $\tau_1 = \tau_2$ , with  $\tau_1$  and  $\tau_2$  referring to the length of the cavity arms. The active gain and absorber chips are equipped with a highly reflective distributed Bragg reflector at the bottom side of the chip. The out-coupling facet has a reflectivity of 99% and is indicated by the lens shape. The propagating electric field is marked by the colored arrows indicating the propagation direction, with the forward direction in light red and backward direction in light blue.

material polarization effects, we eliminate the polarization adiabatically. We then follow a similar procedure as proposed in Ref. [33], taking into account both propagation directions of the electric field inside the cavity and integrate along the characteristic curves for each section of the cavity. A detailed description of the derivation is given in Appendix A.

In contrast to previous DDE models for passively mode-locked VECSELs [28,31], we do not approximate the VECSEL by a ring cavity as we include both propagation directions. Furthermore, for a qualitative study of the pulse cluster dynamics it is sufficient to exclude microscopic effects as opposed to Refs. [24–26].

The investigated VECSEL consists of a SESAM, a gain-chip and an out-coupling facet. The components are positioned in a V-shaped geometry as shown in Fig. 1 and as experimentally realized [18,19]. We assume the width of the active sections (quantum wells) in the gain and SESAM chip to be infinitesimally small [33]. The regions between the gain and SESAM are included as two passive sections, not affecting the electric field. Due to the normal incidence at the SESAM in the experimental setup of the semiconductor chips [18], the active region of the SESAM is passed twice at approximately the same time. Additionally, the limited bandwidth of the gain is modeled by a Lorentzian filter at the out-coupling facet. Taking these assumptions into account, we derive a system of multidelay differential equations describing the dynamics of the dimensionless electric field  $E(t) = E^+(t, z = 0)$  at the out-coupling facet and the carrier dynamics in the gain  $G(t)$  and the absorber section  $Q(t)$ . On account of reducing the number of delays in the DDE model [19], the dynamic variables of carrier densities in the gain  $G(t)$  and the saturable absorber  $Q(t)$ , are transformed to the co-moving frame of the forward propagating field. This leads to the following set of DDEs for our bifurcation analysis, modeling the dynamics of  $E(t)$ ,  $G(t)$ , and  $Q(t)$ :

$$\frac{dE}{dt} = -\gamma E(t) + \gamma E(t - T)R(t - T), \quad (1)$$

$$\begin{aligned} \frac{dG}{dt} = J_g - \gamma_g G(t) - [e^{G(t)} - 1] \\ \times [ |E(t)|^2 + |E(t - 2\tau_2)|^2 e^{2Q(t-2\tau_2)+G(t-2\tau_2)} ], \end{aligned} \quad (2)$$

$$\frac{dQ}{dt} = J_q - \gamma_q Q(t) - r_s [e^{2Q(t)} - 1] e^{G(t)} |E(t)|^2, \quad (3)$$

$$R(t - T) = \sqrt{\kappa} e^{\frac{1-i\alpha_g}{2} [G(t-2\tau_1)+G(t-T)] + (1-i\alpha_q)Q(t-T)}, \quad (4)$$

where  $\gamma$  is the gain bandwidth modeled by the linewidth of the Lorentzian filter,  $\gamma_{g,q}$  are the nonradiative carrier recombination rates in the gain and the absorber section,  $J_g$  is the pump current in the gain section (normalized so

that  $J_g = 0$  corresponds to transparency),  $J_q$  refers to the unsaturated absorption in the absorber section,  $\kappa$  represents the nonresonant losses per round trip,  $r_s$  is proportional to the ratio of the differential gain coefficients in the gain and absorber section, and  $\alpha_{g,q}$  are the linewidth enhancement factors in the gain and absorber section, respectively.

The delays  $\tau_1$  and  $\tau_2$  are defined by the length of the corresponding cavity arm as indicated in Fig. 1. Consequently, the cold-cavity round-trip time is defined as  $T = 2(L/v_g) = 2\tau_1 + 2\tau_2$ , where  $v_g$  is the group velocity of the electric field and  $L$  corresponds to the spatial length of the cavity. The term  $R(t - T)$  defined by the algebraic Eq. (4), gives the total amplification and losses of the electric field during one round trip in the V-shaped resonator. In comparison to the works assuming a circular geometry for monolithic mode-locked lasers [13,34–36], it includes three field-carrier interaction terms, namely  $[G(t - 2\tau_1), G(t - T)]$  and  $Q(t - T)$ . These are characterized by the (delayed) gain and absorption terms in the exponential. Specific for the V-shaped cavity, the gain chip is passed twice per round trip at two different points in time. The interaction with the active section of the SESAM during one round trip is reduced to two interactions at the same time, due to the negligible spatial extent of the active region. This results in a factor of 2 in front of the SESAM carrier term  $Q(t - T)$  in the exponential in Eq. (4).

The parameters used in this work are chosen to adapt experimental values [18,19] and are given in Table I. We perform our bifurcation analysis at values of  $\alpha_{g,q} = 0$  for several reasons. Firstly, it has been found that the dynamical  $\alpha$  factor approaches 0 for short optical pulses in quantum-well as well as in quantum-dot lasers [37,38]. The reason for that lies within the delay of the refractive index change induced by a short pulse. The index change at the optical frequency of the exciting pulse occurs only after it has already passed the active medium. Secondly, we are aiming at a qualitative description of the geometric effect underlying the formation of pulse clusters and it has been shown that similar DDE models provide an excellent qualitative agreement with experimentally determined dynamics [36,39,40] with the  $\alpha$  factor set to 0. Thirdly, we investigate the numerically found dynamics also for a variety of  $\alpha$  factors and the general structure of the dynamical regimes did not change drastically (see Appendix B).

TABLE I. Parameter values used in the bifurcation analysis. Parameters chosen to adapt experimental values [18,19].

Symbol	Value	Symbol	Value
$J_q$	$-104 \text{ ns}^{-1}$	$\gamma$	$240 \text{ ns}^{-1}$
$\gamma_g$	$1 \text{ ns}^{-1}$	$\gamma_q$	$150 \text{ ns}^{-1}$
$\alpha_g$	0	$\alpha_q$	0
$\kappa$	0.99	$r_s$	2

We start our investigations for cavities with a round-trip times of  $T = 193 \text{ ps}$ , which are comparatively low for these types of VECSELs, but help to generate a first understanding of the dynamics. In the following we then increase the round-trip time up to the region where  $\gamma_g T > 1$ , which can lead to the occurrence of localized states [28,30]. The results presented in the first sections of this work are based on a symmetric arrangement of gain and absorber chip in the cavity ( $\tau_1 = \tau_2$ ). Thus, it is possible to rule out that the pulse cluster dynamics emerge due to an asymmetry of the external cavity.

For the bifurcation analysis presented in the following section the path continuation software package DDE-Biftool [41] is used. Furthermore, numerical solutions of the DDE system are obtained by utilizing customized numerical integration software based on the Runge-Kutta algorithm of fourth order.

### III. RESULTS

#### A. Emergence of the pulse cluster solution branch

As a starting point of our bifurcation analysis we find an algebraic expression for the fixed point of cw lasing of the form:

$$(E, G, Q) = (E_0 e^{i\omega t}, G_0, Q_0), \quad (5)$$

similar to Refs. [13,34,42], with  $\omega$  corresponding to the frequency of the longitudinal mode relative to the maximum gain. Substituting Eq. (5) into Eqs. (1)–(3) yields the following set of algebraic equations for the different monochromatic solutions of the cw steady state:

$$\omega^2 = \kappa \gamma^2 e^{2G_0+2Q_0} - \gamma^2, \quad (6)$$

$$\frac{\omega}{\gamma} = -\tan(\alpha_g G_0 + \alpha_q Q_0 + \omega T) \quad (7)$$

$$G_0 = \frac{1}{\gamma_g} [J_g - (e^{G_0} - 1)(|E_0|^2 + |E_0|^2 e^{2Q_0+G_0})], \quad (8)$$

$$Q_0 = \frac{1}{\gamma_q} [J_q - r_s (e^{2Q_0} - 1) e^{G_0} |E_0|^2]. \quad (9)$$

The threshold current  $J_g = J_{\text{th}}$  of the maximum gain cw lasing steady state (relative to the transparency current  $J_{\text{th}} = J_{\text{abs,th}} - J_{\text{abs,trans}}$ ) can be defined as the bifurcation point in which the fixed-point solution of the off state  $(0, G_0, Q_0)$  becomes unstable [13,43]. In the following analysis, the pump current is given relative to the threshold current  $J_{\text{th}}$ . We remark that there is no one-to-one correspondence between experimental pump powers and the value of  $J$ . Due to the parameter normalization in the model, a numerical pump current of  $J = 30 J_{\text{th}}$  corresponds to approximately seven times the physical threshold current. We find an expression for  $J_{\text{th}}$  by substituting Eq. (6)

and Eq. (9) into Eq. (8)

$$J_{\text{th}} = \gamma_g \left[ -\frac{1}{2} \ln(\kappa) - \frac{J_g}{\gamma_q} + \frac{1}{2} \ln \left( 1 + \frac{\omega^2}{\gamma^2} \right) \right]. \quad (10)$$

At this value for  $J_g$  the cw solution inhibiting the lowest detuning from the maximum gain, i.e.,  $\omega = 0$ , becomes stable. As the mode-locking solutions of interest bifurcate from this solution we only investigate  $\omega = 0$  in the following. The corresponding input-output curve for cw emission is shown as a dashed line in Fig. 2(a). As for ring cavity lasers [34,44], a series of Andronov-Hopf bifurcations can be found along this cw branch (in pump power  $J_g$ ) by calculating the dominant eigenvalues (EV). At these Hopf bifurcation points, harmonic mode-locking branches emerge, which we follow by numerical path continuation. They can be distinguished according to the period of the solution born in the respective bifurcation point ( $T_{\text{period}} \approx T/N$ , where  $N$  corresponds to the order of the Hopf bifurcation). The spacing (in  $J_g$ ) and total number of Hopf bifurcations along the branch is governed by the gain bandwidth  $\gamma$  and the round-trip time  $T$ . These parameters also determine the pulse width of the periodic solutions. We choose  $\gamma = 240 \text{ ns}^{-1}$ , two magnitudes smaller than the experimental values, in order to achieve reasonable computation times without drastically changing the underlying dynamics emerging from the first Hopf bifurcations. We remark that the qualitative bifurcation mechanisms remain unchanged for larger values (up to  $\gamma = 1600 \text{ ns}^{-1}$ ).

On the account of finding fundamental pulse cluster solutions with a period approximately equaling the cold cavity round-trip time as observed in experiments [19,20], we first investigate the solution branch bifurcating from the first Hopf bifurcation ( $H_1$ ) of the cw solution. The result is shown as a solid line in Fig. 2(a), with thick regions indicating stable solutions, i.e., experimentally observable emission dynamics. We find stable fundamental mode locking [Fig. 2(b<sub>3</sub>)] directly after the  $H_1$  bifurcation point, similar to the case of a circular cavity. As the pump power is increased, the FML solution becomes unstable in the  $SN_{1u}$  saddle-node bifurcation. Here the first subscript refers to the number of pulses contained in the pulse cluster and the second subscript serves as an identifier to distinguish the saddle-node bifurcations according to their position along the branch ( $SN_{\text{nu}}$  upper saddle node,  $SN_{\text{nl}}$  lower saddle node). At the  $SN_{1u}$  point a side pulse emerges [see profile Fig. 2(b<sub>2</sub>)], and closely after this bifurcation point, the number of unstable eigendirections is turned to three in a torus bifurcation (not shown). Following the solution branch, the two pulses grow closer together in amplitude and temporal spacing, forming a two-pulse cluster beyond the  $SN_{2l}$  bifurcation point. This bifurcation leads to a change from three unstable to two unstable eigenvalues. The resulting pulse cluster solution

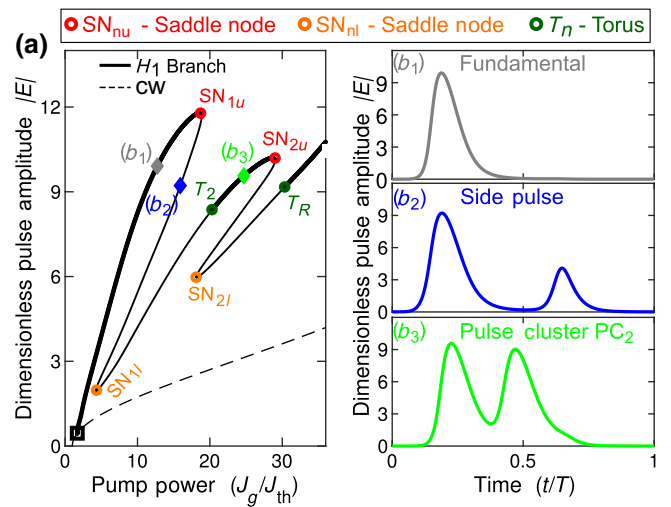


FIG. 2. (a) Maximum electric field amplitude along the  $H_1$  periodic solution branch (solid line), emerging from the first Hopf bifurcation of the cw steady state (dashed line) for increasing pump power. The pump power is normalized to the lasing threshold  $J_{\text{th}}$ , the pulse amplitude is dimensionless. Stable (unstable) solutions are indicated by thick (thin) lines. Red (orange) circles mark saddle-node bifurcations  $SN_{\text{nu}}$  ( $SN_{\text{nl}}$ ) that change the stability at the top (bottom) of the loops. The first subscript refers to the number of pulses in the cluster. Torus bifurcations  $T_n$  are indicated in green. (b<sub>1</sub>) Electric field profile for one period of the stable fundamental mode-locking solution, marked by the gray diamond in (a). (b<sub>2</sub>) Pulse profile of the unstable side pulse emerging shortly before the saddle-node point  $SN_{1u}$ , marked by the blue diamond. (b<sub>3</sub>) Stable pulse cluster solution ( $PC_2$ ) marked with the green diamond. Round-trip time  $T = 193 \text{ ps}$ , all other parameters as given in Table I.

is still unstable and contains two pulses ( $PC_2$ ). It is stabilized in a torus bifurcation ( $T_2$ , subscript referring to the number of pulses in the cluster). The corresponding stable electric field profile is shown exemplary in Fig. 2(b<sub>3</sub>). The stable  $PC_2$  dynamics is again bound by a saddle-node bifurcation ( $SN_{2u}$ ) at larger pump powers [Fig. 2(a)]. Beyond  $SN_{2u}$ , the solution undergoes a similar bifurcation scenario as the FML solution before. Thus, an additional, third, pulse emerges within the pulse profile. After passing the  $SN_{2l}$  point, the pulses merge and a stable region of single-pulse mode locking, characterized by temporally wide pulses (pulse width approximately equal to 0.4T), remains and becomes stable in a torus bifurcation ( $T_R$ ). This dynamics remains stable for a wide range of pump powers and due to the width of the pulses there is a continual field-carrier interaction in the gain. In order to unravel changes of the dynamics induced by the cavity length, the  $H_1$  branch is continued in pump power for different round-trip times ( $T = 190 \text{ ps}$ – $T = 1 \text{ ns}$ ). At this point we stress that the symmetry of the cavity is kept fixed, i.e., the length of the cavity arms is equally enlarged ( $\tau_1 = \tau_2$ ).

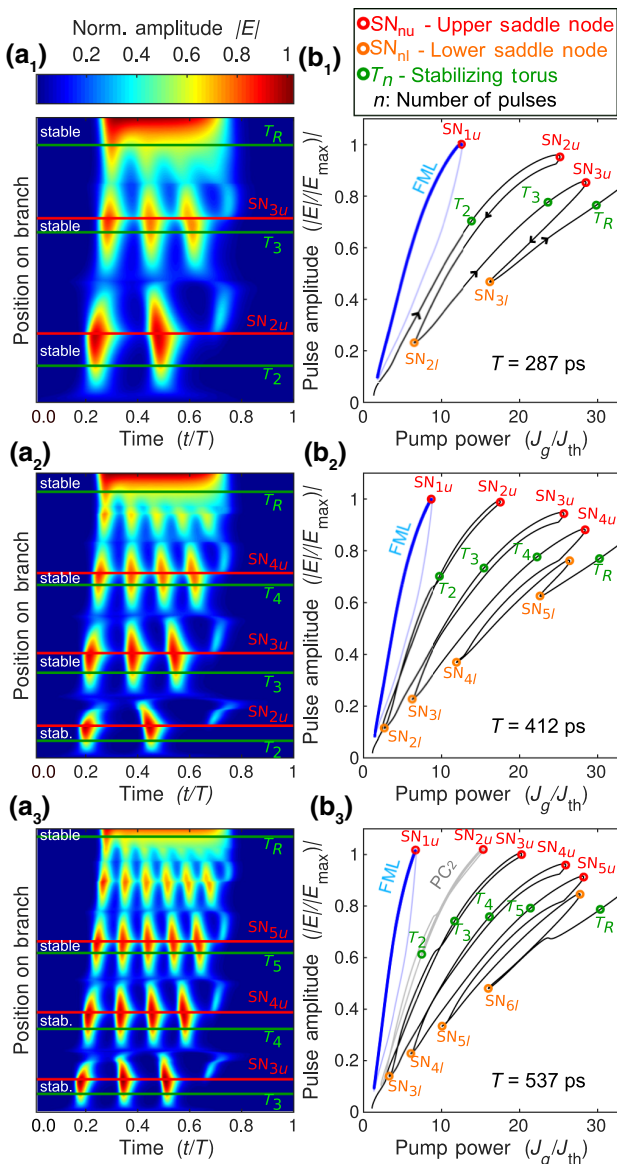


FIG. 3. (a<sub>1</sub>-<sub>3</sub>): Normalized electric field amplitude profiles along the fundamental  $H_1$  branch plotted as color code for round-trip times of  $T = 287$  ps (a<sub>1</sub>),  $412$  ps (a<sub>2</sub>) and  $537$  ps (a<sub>3</sub>). The  $x$ -axis corresponds to one period of the periodic solution whereas the  $y$ -axis represents the position on the branch. (b<sub>1</sub>-<sub>3</sub>): Maximum electric field amplitude along the solution branch emerging from the  $H_1$  Hopf bifurcation for the same round-trip times as in (a<sub>1</sub>-<sub>3</sub>). Torus bifurcations are marked in green, saddle-node bifurcations in red lines. Orange circles represent saddle-node bifurcations, which lead to the disappearance of one unstable EV, with a minimum of 2 unstable EVs after the bifurcation. Nomenclature as described in the text. The detached fundamental mode-locking solution is indicated in light blue, the detached  $PC_2$  region is shown in gray (b<sub>3</sub>). All other parameters chosen as in Table I.

In Fig. 3(a) we show a 2D plot of one period of the normalized electric field amplitude for each point along the  $H_1$  branch, while the corresponding maximum amplitude

along the solution branches are shown in Fig. 3(b) for three different round-trip times (from top to bottom:  $287$ ,  $412$ , and  $537$  ps). The bright red features in the color plots [Fig. 3(a)] indicate the maximum pulse amplitudes and thus the changes of the temporal pulse positions following the upper saddle-node bifurcations (red lines) can nicely be seen. As the round-trip time is increased, the general form of the branch with subsequent looping solutions stays similar to what is observed in Fig. 2. Nevertheless, the number of loops created along the branch increases, which corresponds to an emergence of higher-order pulse clusters. This can be seen in the color plots where up to six peaks can be found in the electric field profile of the laser emission [see Fig. 3(a<sub>1</sub>-<sub>3</sub>)]. The more pronounced looping behavior is based on the emergence of further pairs of saddle-node bifurcations ( $SN_{nu}$  and  $SN_{nl}$ ) along the branch. Physically this can be attributed to the higher round-trip times allowing for lower pulse widths and therefore a higher number of pulses in the cavity. In analogy to the case of low round-trip times discussed in Fig. 2, the upper saddle-node bifurcations ( $SN_{nu}$ , red) change the dynamics from stable to unstable, whereas in the lower ones ( $SN_{nl}$ , orange) a minimum number of two unstable eigenvalues can be found after the bifurcation.

The higher-order PCs continuously develop along the branch with increasing  $T$ . Their formation starts with an additional side pulse emerging at the upper saddle-node bifurcations [ $SN_{nu}$ , red lines in Fig. 3(a<sub>1</sub>-<sub>3</sub>)], of the previous loop and then similar to the mechanism explained for the  $PC_2$  move closer together until they finally stabilize in a torus bifurcation. By inspecting the color codes in Fig. 3(a) we examine that the pulse amplitudes and the temporal interpulse distances continuously adjust along the branch (bright spots move close to each other). The temporal distance between the pulses in the stable regions of the pulse clusters is given by  $T_{dist} \approx T_{period}/2N_p$ , where  $N_p$  corresponds to the number of pulses in one cluster. The regimes of stable higher-order  $PC_n$  dynamics [solid lines in Fig. 3(b<sub>1</sub>-<sub>3</sub>)] are bound by torus bifurcations at low pump powers (green circles) and  $SN_{nu}$  saddle-node bifurcations (red circles) at higher pump powers, respectively. This means that only the small regions of the solution branch in between the red and the green circles are stable, and thus observable experimentally. Note that although we find the solutions well separated along the branch they actually occur at similar pump powers [see Fig. 3(b)], which means that they are multistable for one point of operation. However, the higher-order  $PC_n$  solutions are initially unstable, as can be seen, e.g., for the  $PC_6$  solution in Fig. 3(a<sub>3</sub>). The corresponding loop along the branch is also already visible in this case [Fig. 3(b<sub>3</sub>)]. As observed for low-cavity round-trip times, the pulses of the highest order  $PC_n$  merge to a single pulse at a certain pump power ( $J_g/J_{th} > 30$ ). Hence, a region of single-pulse mode locking with a wide pulse becomes stable [large red feature at the top of Fig. 3(b<sub>1</sub>-<sub>3</sub>)]

in a torus bifurcation ( $T_R$ ), at large  $J_g$ . This solution eventually occurs for all considered round-trip times ( $T < 1200$  ps). Another effect induced by increasing the round-trip time is the detaching of lower-order PC solutions from the  $H_1$  branch. These subsequently become solitary branches as exemplary shown in Fig. 3(b<sub>1</sub>) for the FML (light blue) and in Fig. 3(b<sub>3</sub>) for the PC<sub>2</sub> (gray) solution. However, the stable dynamical regions are not affected by this mechanism and thus from an experimental point of view it is not visible. Nevertheless, it is crucial information for discussing the origin of solutions, as the connection to the  $H_1$  branch only exists for low  $T$ .

The bifurcation scenarios governing the detaching of the PC branches as well as the ones leading to the emergence of higher-order pulse clusters will be discussed in the next two sections.

## B. Two-parameter bifurcation diagram in the ( $J_g$ , $T$ ) plane

The underlying mechanism determining the evolution of higher-order pulse cluster dynamics is found to be similar for all investigated clusters and can be unraveled by continuing the saddle-node and torus bifurcations, which confine the stable regions of the PC <sub>$n$</sub>  solutions, in ( $J_g$ ,  $T$ ) parameter space. It is already visible from the development of the  $H_1$  branch with increasing round-trip time in Fig. 3(b), that PCs emerge from pairs of saddle-node bifurcations (SN<sub>nu</sub> and SN<sub>nl</sub>) enclosing the corresponding loop along the  $H_1$  branch. Following them in the ( $J_g$ ,  $T$ ) plane leads to the bifurcation diagram shown in Fig. 4(a). The red/orange lines represent the SN<sub>nu</sub> (SN<sub>nl</sub>) bifurcations. Each pair of saddle-node bifurcations vanishes in the cusp bifurcation point, characterized as the point where the saddle-node lines of the lower and upper loop merge. The position of this point decreases in pump power and increases in round-trip time with the number of pulses in the corresponding PC <sub>$n$</sub>  solution. As the PC <sub>$n$</sub>  solutions can only exist in the regions enclosed by the corresponding SN lines, all PC solutions eventually disappear for high enough pump powers (see the right of Fig. 4). Following the pairs of saddle-node bifurcations to higher round-trip times, we see that they rapidly separate directly after the cusp point. Therefore, the emerging loop along the  $H_1$  branch grows in width in this region. However, at only slightly higher  $T$ , the upper-loop SN<sub>nu</sub> line folds back in pump power and asymptotically approaches the  $H_1$  line [black line in Fig. 4(a)], which can also be observed for the SN<sub>nl</sub> lines. Therefore, the position of the saddle-node pairs approaches the same values in  $J_g$ . Hence, a large number of stable PC solutions exists simultaneously at higher cavity round-trip times, confined in a small interval of pump powers. The looping behavior of the solution branch leads to an almost vertical orientation of the corresponding loops between the bifurcation points as exemplary shown for the

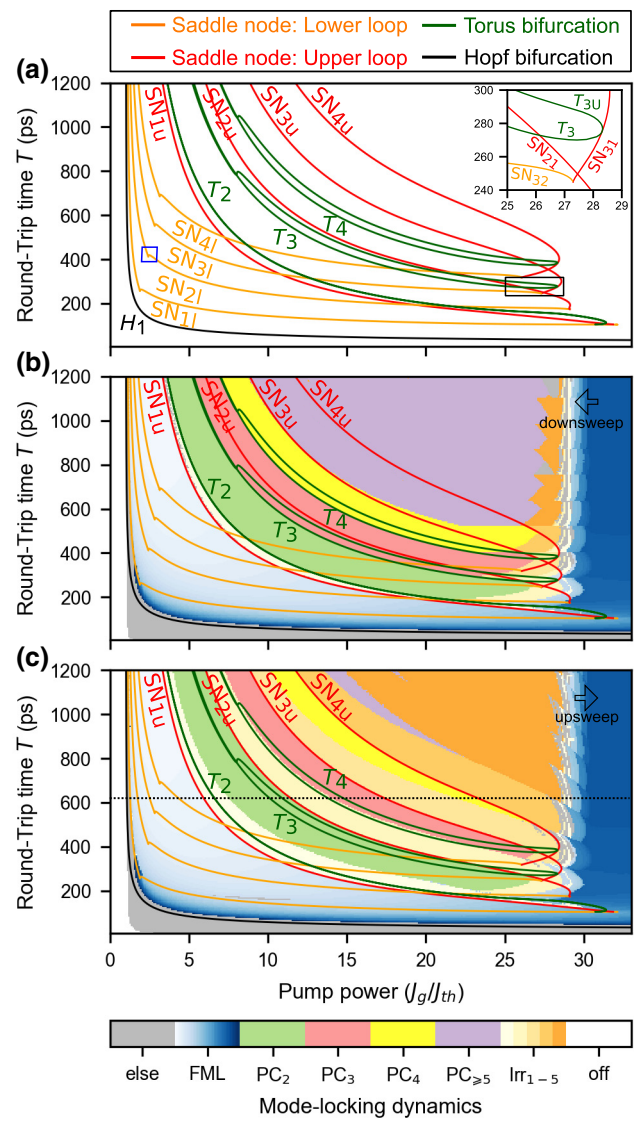


FIG. 4. Two-parameter bifurcation diagram in the ( $J_g$ ,  $T$ ) plane. (a) Path continuation of the saddle-node SN<sub>nu</sub> (SN<sub>nl</sub>) bifurcations, corresponding to the upper (lower) loop (see Fig. 3) plotted in red (orange). Torus-bifurcation lines  $T_n$  are marked in green. The black line refers to the first Hopf bifurcation of the cw steady state. (b),(c) Numeric up and downsweep showing the underlying dynamics indicated by the color code, with FML corresponding to fundamental mode locking with low pulse width encoded in light blue and wide pulses repeating at a fundamental frequency in dark blue, PC <sub>$n$</sub>  refers to pulse clusters containing  $n$  pulses, Irr<sub>1-5</sub> corresponds to irregular pulse clusters, where light yellow represents one pulse and orange a minimum of five pulses in the irregular cluster (see Fig. 5). An enlargement of the blue rectangle in (a) is shown in Fig. 7.

FML solution in Fig. 3(b<sub>3</sub>). The findings of the bifurcation analysis are underlined by numerical calculations shown in Figs. 4(b) and 4(c). The numeric upsweep indicates that the upper stability boundary of the PC <sub>$n$</sub>  regions is given by the SN<sub>nu</sub> lines. This can nicely be seen in Fig. 4(c), with PC<sub>2</sub>

dynamics in light green,  $PC_3$  dynamics in light red,  $PC_4$  dynamics in yellow, and pulse clusters with five or more pulses  $PC_{>5}$  in purple. The different dynamical regions detected along one upsweep at  $T = 625$  ps are displayed in Fig. 5 as space-time plots that show the laser emission over many round trips. If the pump power is swept past a saddle-node stability boundary in  $J_g$  ( $SN_{nu}$ ), the dynamics does not directly jump onto the next stable pulse cluster attractor. Instead irregular pulse clusters emerge first, which are characterized by a higher pulse width and a temporal drift [see Figs. 5(b), 5(d), 5(f), 5(h), and 5(i)]. They are color coded in Fig. 4(c). These regions with irregular dynamics most likely originate from the high degree of multistability.

At low round-trip times ( $T < 170$  ps), no pulse cluster dynamics are present. Only the mode-locked solution corresponding to wide pulse emission [dark blue region in Figs. 4(b) and 4(c)] directly emerges from the  $H_1$  Hopf bifurcation. This changes as the first loop emerges from a cusp of saddle-node bifurcations ( $SN_{1u}$  and  $SN_{1l}$ ), leading to stable of narrow FML pulses. The transition from wide pulse FML to narrow pulse-width FML is indicated by the

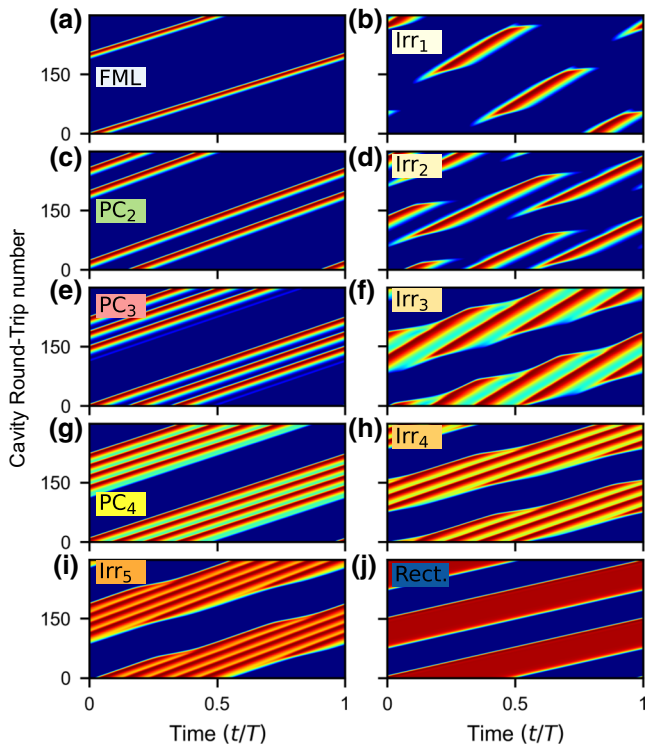


FIG. 5. Pseudo space-time plot of the electric field amplitude in the different dynamic regimes for pump powers along an upsweep at  $T = 625$  ps, marked by the black dotted line in Fig. 4(c). The color code is the same as in Fig. 3 on a logarithmic scale. Each plot shows 300 round trips after a transient time of 30000 round trips. The time is normalized to the cavity round-trip time. The pump power values  $J_g/J_{th}$  are as follows: (a) 4, (b) 6.5, (c) 10, (d) 12.5, (e) 15, (f) 20, (g) 22, (h) 25, (i) 28, and (j) 32.

blue shading in Figs. 4(b) and 4(c), light blue refers to narrow widths of  $0.01T$ , while dark blue marks pulse widths of  $0.35T$ . The  $T_2$  torus emerges from a 1:1 resonance scenario close to the SN cusp point at  $J_g \approx 30.8$ ,  $T \approx 105$  ps and builds the boundary between FML with side pulses and wide-pulse emission. However, with increasing cavity round-trip times further torus points emerge along the branch and hence the upper boundary (transition to wide-pulse emission) is characterized by different torus bifurcations as  $T$  is increased. At this point we want to stress that the threshold pump power in our model is defined relative to the transparency value, which is set to  $J_g = 0$ . In Ref. [18], the gain chip was found to be transparent at an optical pump power of  $P_{abs,trans} = 10$  kW/cm<sup>2</sup>, with a lasing threshold of approximately  $P_{abs,th} = 13$  kW/cm<sup>2</sup> and the experiments were performed at a pump power of  $P_{abs,pump} \approx 60$  kW/cm<sup>2</sup>, which corresponds to  $J_g = 20J_{th}$  in our model.

The lower stability boundary of the FML dynamics is given by the  $H_1$  bifurcation. At higher round-trip times the FML solution detaches from the  $H_1$  branch and the stable FML regions are then confined by the  $SN_{1u}$  and  $SN_{1l}$  bifurcations. Two enlargements of the  $(J_g, T)$  plane, marked by the blue and black rectangles in Fig. 4(a), are elucidated in the following to get a better insight into the organizing bifurcation scenarios of the stable pulse cluster solutions. At first we elaborate how the stabilizing  $T_n$  torus bifurcations emerge for the different pulse cluster solutions and then the detaching of solution branches are discussed.

### 1. Emergence of torus bifurcations

Although the  $PC_n$  loops develop in cusps of saddle-node bifurcations, stable dynamics can only be found above the round-trip time at which the respective stabilizing torus bifurcation  $T_n$  (dark green lines Fig. 4) emerges. These bifurcations also characterize the lower stability boundary of the PCs as shown in the numeric downsweep in Fig. 4(b). For the  $PC_2$  solution, the stabilizing  $T_2$  bifurcation emanates at lower round-trip times than the saddle-node bifurcations bounding the corresponding branch loop ( $SN_{2u}$ ,  $SN_{2l}$  cusp point). Therefore, a stable  $PC_2$  region can be found directly above the  $SN_{2u}$ ,  $SN_{2l}$  cusp point in the  $(J_g, T)$  plane, with the lower boundary given by the  $T_2$  bifurcation line. For the  $PC_3$  dynamics, we find a different stabilizing behavior, as we can see in the inset of Fig. 4(a) showing a close up of the region marked by a black square. Here the  $T_3$  bifurcation emanates from a torus-torus connection point ( $T_3-T_{3u}$ ). In Fig. 6 we separately concentrate on the bifurcations around this connection point with Fig. 6(a) again showing an enlargement into the  $(J_g, T)$  plane. The blue lines indicate the round-trip times at which the pulse amplitudes along the  $H_1$  branch are shown in the subplots (b)–(e) of Fig. 6. As the torus lines do not exist

for round-trip times below the connection point [Fig. 6(b)], we only find unstable  $PC_3$  dynamics along the  $H_1$  branch [see Fig. 6(b)]. At the connection point [see Fig. 6(c)], the two torus bifurcations ( $T_3$  and unstable  $T_{3u}$ ) emerge along the branch and enclose a stable  $PC_3$  region. They separate with increasing round-trip time [see Fig. 6(a)] and the width of the stable region increases in pump power. As we continue the  $T_{3u}$  bifurcation to higher round-trip times, it loops back to lower pump powers. This leads to the  $T_{3u}$  bifurcation point passing the  $SN_{3u}$  point along the branch [see Fig. 6(d)] resulting in the previously discussed confinement of the stable regions by torus and SN bifurcations. Further torus bifurcations stabilizing PCs with more than three pulses also emerge from torus-torus connection points as can be seen from the  $T_4$  line in Fig. 4, with a mechanism similar to the case discussed in Fig. 6.

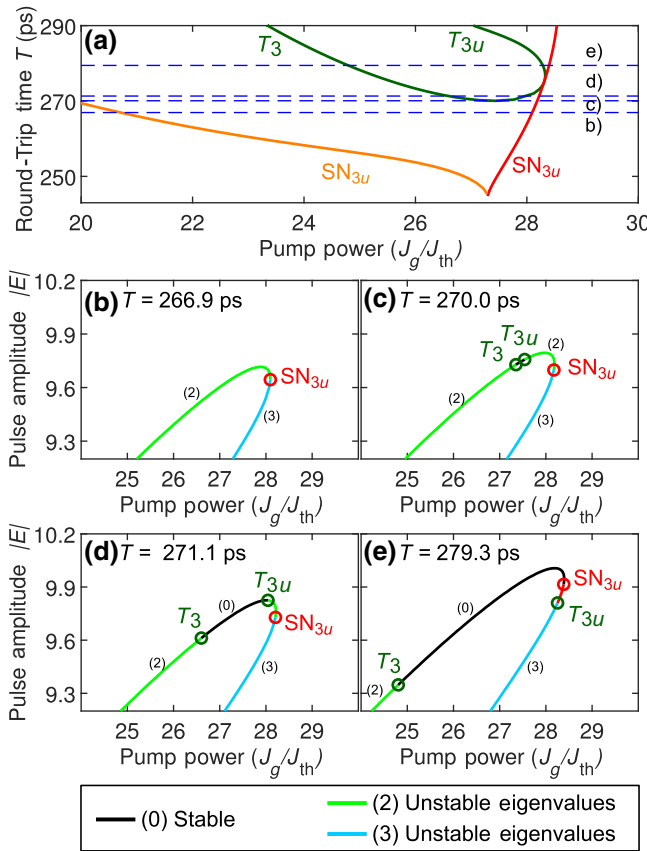


FIG. 6. (a) Close up of the two-parameter bifurcation diagram in the  $(J_g, T)$  plane, showing the torus connection point marked as a black rectangle in Fig. 4(a). Blue lines indicate the round-trip times at which the maximum pulse amplitude along the  $H_1$  solution branch in the region of  $PC_3$  dynamics is shown in (c)–(e). The number of unstable EVs is indicated by the numbers and is color coded with (0) unstable EVs in black, (2) unstable EVs in green, and (3) unstable EVs in cyan. The  $SN_{3u}$  saddle-node point is marked as a red circle, torus bifurcations as green circles. Other parameters as given in Table I.

## 2. Detaching of solution branches

With increasing round-trip time the emergence of higher-order pulse cluster solutions is accompanied by a detaching of lower-order PCs as well as the FML solution from the  $H_1$  branch [see Fig. 3(b)], which then further exist as solitary branches. The bifurcation scenario leading to this effect can be unraveled by investigating cusps of saddle-node bifurcations along the  $SN_{nl}$  lines. One of these cusps is marked exemplary in Fig. 4(a) by a blue square and a close up is shown in Fig. 7(a). For round-trip times below the cusp point [marked in yellow in Fig. 7(a)], the  $PC_2$  solution is connected to the  $H_1$  branch and at the lower loop only the  $SN_{2l}$  bifurcation exists as can also be deduced from the plotted amplitudes for increasing  $J_g$  in Fig. 7(e). Above the cusp point, two saddle-node bifurcations ( $SN_{2a}$ ,  $SN_{2b}$ ) emerge, which are also observable as two additional curves in the electric field amplitudes along the branch[Fig. 7(d)]. At a distinct cavity size, marked by the transition from white to red background in Fig. 7(a), the  $SN_{2a}$  bifurcations collides with the  $SN_{2l}$  bifurcation at the lower loop of the solution branch. This results in a degenerate saddle-node point (unfolding of transcritical bifurcation) in which the pulse cluster solution is still attached to the  $H_1$  branch [see Fig. 7(c)]. For higher round-trip times the  $SN_{2a}$  and  $SN_{2l}$  bifurcations vanish and hence the pulse cluster solution becomes an independent branch [see Fig. 7(b)]. This mechanism is observable for the fundamental mode-locking solution as well as for higher-order

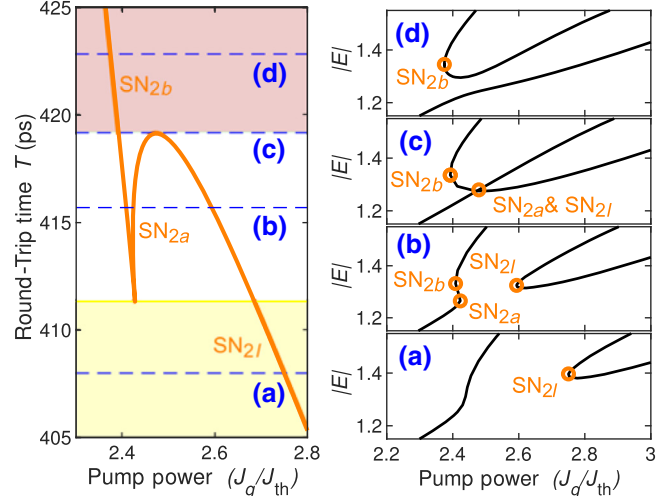


FIG. 7. Close up of the two-parameter  $(J_g, T)$  bifurcation diagram in the region of the blue square in Fig. 4(a). The orange line depicts the saddle-node bifurcations and C marks the cusp point. Red-shaded background corresponds to a detached branch, whereas in the yellow-shaded region the branch is still connected. (b)–(e) Corresponding plots of the solution branch for slices of the round-trip times marked by blue lines in (a), with the SN bifurcations marked with orange circles. Other parameters as given in Table I.

pulse clusters as this kind of saddle-node cusp can also be found along the respective saddle-node lines (see orange lines in Fig. 4). However, as the bifurcations governing the stability of the dynamics are not affected by the detaching, the stable PCs are not changed in this process. However, the lower stability boundary of the FML solution changes with the detaching of the branch as it is given by the  $SN_{1u}$  bifurcation after the detaching and by the  $H_1$  Hopf bifurcation prior to it.

### C. Asymmetric cavity geometry

So far we have only presented results including a symmetric cavity, i.e.,  $\tau_1 = \tau_2$ . In order to further investigate the influence of the cavity geometry, we also look at the case in which the gain chip is moved towards the out-coupling facet or the SESAM, i.e.,  $\tau_1 \neq \tau_2$ , but the total length of the cavity is kept fixed with  $T = 2\tau_2 + 2\tau_1 = \text{const}$ . To visualize the changes to the bifurcation structure induced by the asymmetry we compute scans in the  $(\tau_2, J_g)$  plane (see Fig. 8), where  $\tau_2 = 0.2$  ( $\tau_1 = 0.3$ ) refers to the case of the gain being shifted towards the absorber, while  $\tau_2 = 0.3$  ( $\tau_1 = 0.2$ ) corresponds to a shift towards the out-coupling facet. The length of the cavity arms is normalized to the total round-trip time  $T$ . By investigating the bifurcation lines confining the stable regions of the pulse cluster dynamics, i.e., the saddle-node and torus bifurcations, we can assess that depending on the position of the gain chip, different dynamical regions can be favored. The torus bifurcations (dark green) do not change their position in  $J_g$  when a slight asymmetry is introduced. However, the  $SN_{nu}$  bifurcations move to a maximum value in  $J_g$  for a slightly asymmetric setup. A proper tuning of the cavity geometry could thus be used to increase the pump-power interval for which a chosen pulse cluster (or the FML) solution is stable. The bifurcation structure exhibits a symmetry in  $\tau_2$  about the symmetric cavity case  $\tau_2 = \tau_1$  (see Fig. 8).

This can be explained by the fact that the distance between gain and absorber ( $\tau_2$ ) is still much larger than the relaxation time of the carriers in the SESAM, i.e.,  $\tau_2 \gg \gamma_q^{-1}$ . Hence, for the small shifts of the gain investigated here, there is only a slight difference whether the gain chip is moved towards or away from the SESAM because both propagation directions are included. As the induced asymmetry favors a higher multistability, the direct numerical integration leads to very different forms of dynamics for high pump powers.

It can also be concluded that a slight asymmetric positioning favors FML mode-locking applications as the stability boundary is shifted to higher pump powers. This has been also observed in experiments, as the highest pulse powers in a mode-locked VECSEL were obtained for a slightly asymmetric cavity configuration [18].

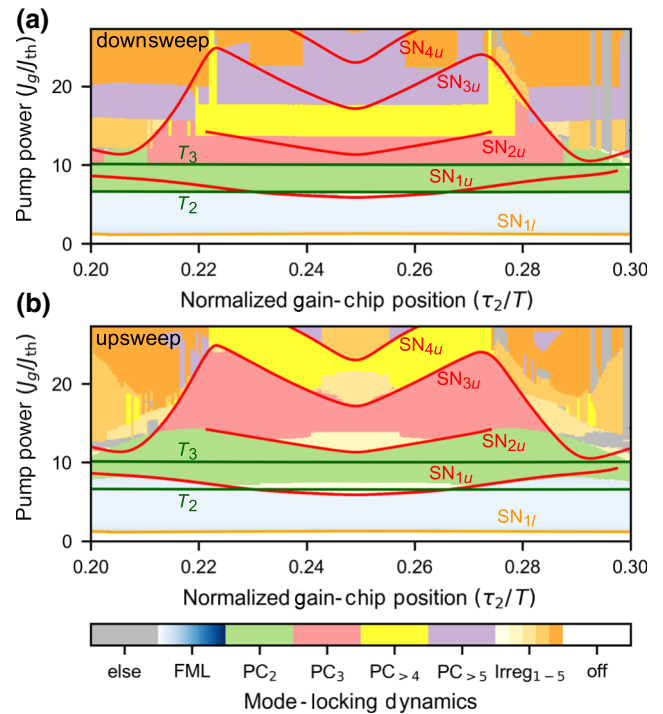


FIG. 8. Regions of pulse cluster emission in the  $(\tau_2, J_g)$  plane, calculated by a numerical downsweep (a) and upsweep (b) in pump power. The gain-chip position  $\tau_2$  is defined with respect to the absorber and normalized to the round-trip time. The color code is the same as in Fig. 4, the blue FML shading is proportional to the pulse width, which is  $0.01T = 6.25$  ps for the values chosen here. The red (orange) lines represent the upper (lower) saddle-node bifurcations, while green lines indicate torus bifurcations. The round-trip time is constant at  $T = 625$  ps. Other parameters as given in Table I.

## IV. CONCLUSION

With our new multidelay differential equation model for passively mode-locked semiconductor lasers with V-shaped cavity geometry, a complete characterization of the dynamics is possible within reasonable computation time. We are able to identify the experimentally found pulse cluster emission of different order and can describe the generating bifurcations. Namely, these are series of saddle-node bifurcations, which lead to a looping behavior of the  $H_1$  solution branch originating from the first Hopf bifurcation of the cw branch. These pulse cluster solutions stabilize in torus bifurcations. Furthermore, increasing the cavity size leads to a detaching of the pulse cluster solutions from the  $H_1$  branch, which makes them hard to identify solely using path-continuation techniques. Thus, numeric integration has to support the analysis. Our results indicate a high degree of multistability between different multipulse solutions. Further we show that certain stable solutions can be favored by introducing an asymmetry to the cavity geometry. This qualitatively reproduces recent

experiments [18], where a slightly asymmetric cavity leads to the best FML performance.

We also find pulse cluster solutions in the parameter regions that allow for the existence of localized states,  $T\gamma_g > 1$ , as found in Refs. [28,29]. Preliminary results indicate that localized states can emerge from the same solution branch as the pulse cluster solutions. In this case, the solution branches of localized states emerging from the Hopf bifurcations along the continuous-wave steady state have a very similar shape as the ones presented in Ref. [28,43]. Additionally, further research has to be conducted regarding the case of a strongly asymmetric cavity [23,45].

To summarize, our results enable the control of the laser pulse emission from passively mode-locked VECSELs via the tuning of the cavity configuration, as they provide an understanding of the generation of unwanted pulse cluster dynamics.

## ACKNOWLEDGMENTS

We thank L. Jaurigue for her previous work on the model. Furthermore, we thank U. Keller and J. Javaloyes for fruitful discussions. We acknowledge the financial support from the SFB787 funded by the DFG.

## APPENDIX A: DDE MODEL DERIVATION

In order to derive a DDE model, we subdivide our laser into four sections. Two active sections, namely gain and absorber, which have a spatial width of  $\Delta z_g$  and  $\Delta z_q$  (see Fig. 9). The regions neighboring the active sections are assumed to be passive, i.e., have no influence on the electric field. Their optical length is defined as  $\tau_1 \times v_g$  and  $\tau_1 \times v_g$ , with the group velocity  $v_g$ . Specific to this laser the width of the gain and the absorber active sections is much smaller than the fastest timescale of the system  $\Delta z_{g,q} \ll v_g \gamma^{-1}$ , where  $\gamma$  represents the gain bandwidth. We start the derivation of our DDE model from the traveling wave model as introduced in Ref. [46,47], with equations for the forward and backward propagating electric field  $\mathcal{E}^\pm$  and the carrier dynamics  $N(z, t)$ :

$$\left[ \pm \partial_z + \frac{1}{v_g} \partial_t \right] \mathcal{E}^\pm(z, t) = \frac{1 - i\alpha(z)}{2} N(z, t) \mathcal{E}^\pm(z, t), \quad (\text{A1})$$

$$\begin{aligned} \partial_t N(z, t) = & J(z, t) - \gamma(z) N(z, t) - r(z) N(z, t) \\ & \times [|\mathcal{E}^+(z, t)|^2 + |\mathcal{E}^-(z, t)|^2], \quad (\text{A2}) \end{aligned}$$

with the rescaling of the charge carrier density  $n(z, t)$  in the quantum-well active medium  $N(z, t) = g(z)\Gamma(z)[n(z, t) - n^{tr}(z)]$ , the pump term  $J(z, t) = g(z)\Gamma(z)[j(z, t) - \gamma(z)n^{tr}(z)]$ , and the differential gain  $r(z) = g(z)\Gamma(z)v_g$ . Where  $n^{tr}(z)$  is the transparency threshold,  $g(z)$  is the differential gain,  $\Gamma(z)$  is the optical confinement factor,  $\alpha(z)$  is the linear amplitude phase coupling factor,  $j(z, t)$  is the electrical pump current, and  $\gamma(z)$  is the carrier relaxation

rate. Following the ideas published in Ref. [33], we integrate the electric field Eq. (A1) along the characteristics in the active sections. We obtain the following algebraic field propagation equations in the active sections:

$$\mathcal{E}^+(z_{g',q'}) = \mathcal{E}^+(z_{g,q}, t - \Delta t_{g,q}) e^{\frac{1-i\alpha_{g,q}}{2} S_{g,q}(t)}, \quad (\text{A3})$$

$$\mathcal{E}^-(z_{g,q}, t) = \mathcal{E}^-(z_{g',q'}, t - \Delta t_{g,q}) e^{\frac{1-i\alpha_{g,q}}{2} S_{g,q}(t)}, \quad (\text{A4})$$

with the integrated carrier densities in the gain section  $S_g(t) = \tilde{G}(t)$  and absorber section  $S_q(t) = \tilde{Q}(t)$  defined according to

$$S_{g,q} = \int_{z_{g,q}}^{z_{g',q'}} dz N \left( z, t - \frac{\Delta t_{g,q}}{2} \right), \quad (\text{A5})$$

where  $t_{g,q}v_g = \Delta z_{g,q}$  corresponds to the optical length of the respective section and the integral boundaries are defined as indicated in Fig. 9. Additionally we assume the differential gain  $g_g$  ( $g_q$ ), the confinement factors  $\Gamma_g$  ( $\Gamma_q$ ), and the relaxation rate  $\gamma_g$  ( $\gamma_q$ ) to be constant along the gain (absorber) active sections. Using the same steps as proposed in Ref. [33] we obtain the following differential equation for the integrated carrier densities in the different sections. This leads to

$$\begin{aligned} \frac{dS_{g,q}}{dt} = & J_{g,q} - \gamma_{g,q} S_{g,q} - r_{g,q} (e^{S_{g,q}} - 1) \\ & \times [| \mathcal{E}^+(z_{g,q}, t) |^2 + | \mathcal{E}^-(z_{g',q'}, t) |^2], \quad (\text{A6}) \end{aligned}$$

with subscript index  $g$  for the gain section and  $q$  for the absorber section. We model the finite gain bandwidth by applying a Lorentzian spectral filter [ $f(\omega) = \gamma(\gamma + i\omega)^{-1}$ ] in a lumped-element approach localized at the out-coupling facet ( $z = 0$ ), similar to Refs. [34,48]. The filter is implemented by the following boundary condition in the frequency domain:

$$\mathcal{E}^+(0, \omega) = \mathcal{E}^-(0, \omega) f(\omega) \sqrt{\kappa}, \quad (\text{A7})$$

with  $\kappa$  describing the accumulated nonresonant losses per round trip. Transforming Eq. (A8) to the time domain by utilizing the convolution theorem and then taking the total derivative with respect to time  $t$  yields

$$\frac{d\mathcal{E}^+(0, t)}{dt} = \gamma [\mathcal{E}^-(0, t) \sqrt{\kappa} - \mathcal{E}^+(0, t)]. \quad (\text{A8})$$

In order to obtain a single equation for the electric field  $\mathcal{E}^+(t) = \mathcal{E}^+(0, t)$  at the out-coupling facet, we express  $\mathcal{E}^-(0, t)$  in terms of  $\mathcal{E}^+(0, t)$  by using propagation Eqs. (A3) and (A4). Additionally we neglect reflection losses at the absorber and gain chip so that  $\mathcal{E}^+(t, z_{q'}) = \mathcal{E}^-(t, z_{q'})$  at

the absorber. Inserting all boundary conditions and taking the limit  $\Delta z_{g,q} \rightarrow 0$  then leads to

$$\begin{aligned} \mathcal{E}^-(z_0, t) &= \mathcal{E}^+(z_0, t - 2\tau_1 - 2\tau_2) \\ &\times e^{\frac{1-\alpha_g}{2}[\tilde{G}(t-\tau_1)+\tilde{G}(t-2\tau_2-\tau_1)]} \\ &\times e^{(1-i\alpha_q)\tilde{Q}(t-\tau_1-\tau_2)}, \end{aligned} \quad (\text{A9})$$

where  $\tau_1$  and  $\tau_2$  correspond to the propagation times in the cavity arms, as indicated in Fig. 9. Inserting Eq. (A9) into the electric field equation yields

$$\begin{aligned} \frac{dE(t')}{dt'} &= -\gamma E(t') + \gamma \sqrt{\kappa} E(t' - 2\tau_2 - 2\tau_1) \\ &\times e^{\frac{1-i\alpha_g}{2}[\tilde{G}(t'-\tau_1-2\tau_2)+\tilde{G}(t'-\tau_1)]} \\ &\times e^{(1-i\alpha_q)\tilde{Q}(t'-\tau_1-\tau_2)}, \end{aligned} \quad (\text{A10})$$

where we rescale the dynamical variable of the electric field  $E = \sqrt{T}v_{gg}\Gamma_g\mathcal{E}$ , with the cold-cavity round-trip time  $T$ . The time is rescaled as  $t' = t/T$ , rates are rescaled by a multiplication  $T$  [44]. Dynamical equations for the carrier dynamics can be found for  $G$  and  $Q$  by expressing the electric fields  $\mathcal{E}^\pm$  in Eq. (A6) by the electric field at the out-coupling facet using the boundary conditions and the propagation equations. This leads to

$$\begin{aligned} \frac{d\tilde{G}(t')}{dt'} &= J_g - \gamma_g \tilde{G}(t') - [e^{\tilde{G}(t')} - 1] \\ &\times [|E(t' - \tau_1)|^2 + |E(t' - \tau_1 - 2\tau_2)|^2 \\ &\times e^{2\tilde{Q}(t'-\tau_2)+\tilde{G}(t'-2\tau_2)}] \end{aligned} \quad (\text{A11})$$

$$\begin{aligned} \frac{d\tilde{Q}(t')}{dt'} &= J_q - \gamma_q \tilde{Q}(t') - r_s[e^{2\tilde{Q}(t')} - 1] \\ &\times e^{\tilde{G}(t'-\tau_2)} |E(t' - \tau_1 - \tau_2)|^2, \end{aligned} \quad (\text{A12})$$

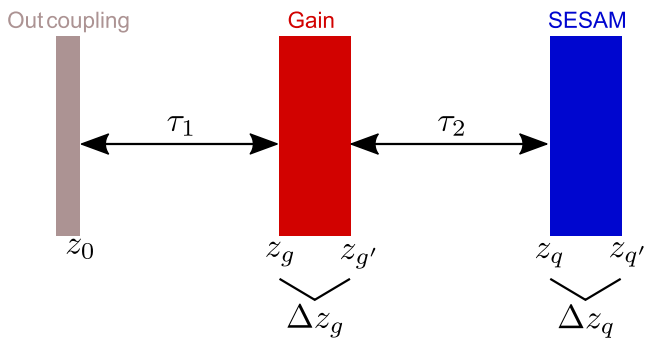


FIG. 9. Sketch of the cavity containing the active sections of gain and absorber with the spatial width of the components denoted as  $\Delta z_g$  and  $\Delta z_q$ .

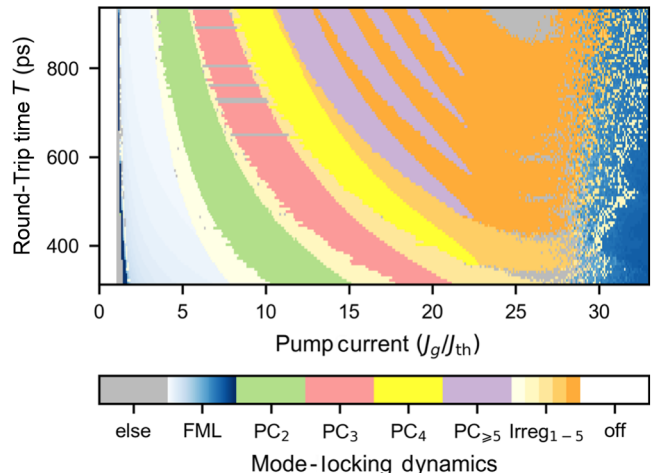


FIG. 10. Two-parameter bifurcation diagram (upsweep in  $J_g$ ) in the  $(J_g, T)$  plane with color code and parameters as described in Fig. 4 except for  $\alpha_g = 2$  and  $\alpha_q = 1$  similar as given in Ref. [18].

where we have introduced the ratio of differential gain coefficients  $r_s = \Gamma_q g_g(\Gamma_g g_g)^{-1} = r_q r_g^{-1}$ . For computational convenience  $\tilde{G}$  and  $\tilde{Q}$  are transformed according to the coordinate transformation  $t' = t + \tau_1$  for Eq. (A11) and  $t' = t + \tau_1 + \tau_2$  for Eq. (A12). We further redefine the variables according to

$$\tilde{G}(t + \tau_1) = G(t), \quad \tilde{Q}(t + \tau_1 + \tau_2) = Q(t). \quad (\text{A13})$$

This leads to the Eqs. (1)–(4).

## APPENDIX B: NONZERO ALPHA FACTORS

On account of investigating the influence of large  $\alpha$  factors on the bifurcation structure, we perform a numerical upsweep for  $\alpha$  factors of  $\alpha_g = 2$  and  $\alpha_q = 1$ , based on the characterization presented in Ref. [18]. The obtained bifurcation diagram is shown in Fig. 10 and it can be seen that the irregular regions between the PC regimes [see Fig. 4(c)] shrink. We remark that the experimentally obtained values resemble static  $\alpha$  factors, which correspond to lower dynamical  $\alpha$  factors, than the exemplarily chosen values. The high dynamical  $\alpha$  factors result in a higher multistability making a numerical analysis more complex, especially at high pump powers.

- [1] A. Schliesser, N. Picque, and T. W. Hänsch, Mid-infrared frequency combs, *Nat. Photonics* **6**, 440 (2012).
- [2] S. M. Link, A. Klenner, and U. Keller, Dual-comb mode-locked lasers: Semiconductor saturable absorber mirror decouples noise stabilization, *Opt. Express* **24**, 1889 (2016).
- [3] T. Udem, R. Holzwarth, and T. W. Hänsch, Optical frequency metrology, *Nature* **416**, 233 (2002).

- [4] S. M. Link, D. J. H. C. Maas, D. Waldburger, and U. Keller, Dual-comb spectroscopy of water vapor with a free-running semiconductor disk laser, *Science* **00**, 00 (2017).
- [5] I. Coddington, N. Newbury, and W. Swann, Dual-comb spectroscopy, *Optica* **3**, 414 (2016).
- [6] K. Lüdge, B. Lingnau, C. Otto, and E. Schöll, Understanding electrical and optical modulation properties of semiconductor quantum-dot lasers in terms of their turn-on dynamics, *Nonlinear Phenom. Complex Syst.* **15**, 350 (2012).
- [7] U. Keller, Recent developments in compact ultrafast lasers, *Nature* **424**, 831 (2003).
- [8] E. A. Avrutin, J. H. Marsh, and E. L. Portnoi, Monolithic and multi-gigahertz mode-locked semiconductor lasers: Constructions, experiments, models and applications, *IEE Proc. Optoelectron.* **147**, 251 (2000).
- [9] R. M. Arkhipov, A. S. Pimenov, M. Radziunas, D. Rachinskii, A. G. Vladimirov, D. Arsenijevic, H. Schmeckebeier, and D. Bimberg, Hybrid mode locking in semiconductor lasers: Simulations, analysis, and experiments, *IEEE J. Sel. Top. Quantum Electron.* **19**, 1100208 (2013).
- [10] K. Y. Lau, I. Ury, and A. Yariv, Passive and active mode locking of a semiconductor laser without an external cavity, *Appl. Phys. Lett.* **46**, 1117 (1985).
- [11] S. Sanders, A. Yariv, J. Paslaski, J. E. Ungar, and H. A. Zarem, Passive mode locking of a two-section multiple quantum well laser at harmonics of the cavity round-trip frequency, *Appl. Phys. Lett.* **58**, 681 (1990).
- [12] O. Solgaard and K. Y. Lau, Optical feedback stabilization of the intensity oscillations in ultrahigh-frequency passively modelocked monolithic quantum-well lasers, *IEEE Photon. Technol. Lett.* **5**, 1264 (1993).
- [13] L. C. Jaurigue, B. Krauskopf, and K. Lüdge, Multipulse dynamics of a passively mode-locked semiconductor laser with delayed optical feedback, *Chaos* **27**, 114301 (2017).
- [14] U. Keller and A. C. Tropper, Passively modelocked surface-emitting semiconductor lasers, *Phys. Rep.* **429**, 67 (2006).
- [15] M. A. Gaafar, A. Rahimi-Iman, K. A. Fedorova, W. Stoltz, E. U. Rafailov, and M. Koch, Mode-locked semiconductor disk lasers, *Adv. Opt. Photonics* **8**, 370 (2016).
- [16] U. Keller, K. J. Weingarten, F. X. Kärtner, D. Kopf, B. Braun, I. D. Jung, R. Fluck, C. Hönninger, N. Matuschek, and J. Aus-der Au, Semiconductor saturable absorber mirrors (SESAM's) for femtosecond to nanosecond pulse generation in solid-state lasers, *IEEE J. Sel. Top. Quantum Electron.* **2**, 435 (1996).
- [17] S. Hoogland, S. Dhanjal, A. C. Tropper, J. S. Roberts, R. Haring, R. Paschotta, F. Morier-Gemoud, and U. Keller, Passively mode-locked diode-pumped surface-emitting semiconductor laser, *IEEE Photon. Technol. Lett.* **12**, 1135 (2000).
- [18] D. Waldburger, S. M. Link, M. Mangold, C. G. E. Alfieri, E. Gini, M. Golling, B. W. Tilma, and U. Keller, High-power 100 fs semiconductor disk lasers, *Optica* **3**, 844 (2016).
- [19] D. Waldburger, C. G. E. Alfieri, S. M. Link, S. Meinecke, L. C. Jaurigue, K. Lüdge, and U. Keller, Multipulse instabilities of a femtosecond SESAM-modelocked VECSEL, *Opt. Express* **26**, 21872 (2018).
- [20] T. Malica, J. Lin, T. Ackermann, D. J. Little, J. P. Toomey, D. Pabœuf, W. Lubeigt, N. Hempler, G. Malcolm, G. Maker, and D. M. Kane, Mapping the dynamical regimes of a SESAM mode-locked vecsel with a long cavity using time series analysis, *Opt. Express* **26**, 16624 (2018).
- [21] S. M. Link, D. Waldburger, C. G. E. Alfieri, M. Golling, and U. Keller, Coherent beam combining and noise analysis of a colliding pulse modelocked vecsel, *Opt. Express* **25**, 19281 (2017).
- [22] A. Laurain, R. Rockmore, H. T. Chan, J. Hader, S. W. Koch, A. R. Perez, W. Stoltz, and J. V. Moloney, Pulse interactions in a colliding pulse mode-locked vertical external cavity surface emitting laser, *J. Opt. Soc. Am. B* **34**, 329 (2017).
- [23] C. G. E. Alfieri, D. Waldburger, S. M. Link, E. Gini, M. Golling, G. Eisenstein, and U. Keller, Optical efficiency and gain dynamics of modelocked semiconductor disk lasers, *Opt. Express* **25**, 6402 (2017).
- [24] I. Kilen, S. W. Koch, J. Hader, and J. V. Moloney, Fully microscopic modeling of mode locking in microcavity lasers, *J. Opt. Soc. Am. B* **33**, 75 (2016).
- [25] I. Kilen, J. Hader, J. V. Moloney, and S. W. Koch, Ultrafast nonequilibrium carrier dynamics in semiconductor laser mode locking, *Optica* **1**, 192 (2014).
- [26] I. Kilen, S. W. Koch, J. Hader, and J. V. Moloney, Non-equilibrium ultrashort pulse generation strategies in VECSELs, *Optica* **4**, 412 (2017).
- [27] J. Mulet and S. Balle, Mode-locking dynamics in electrically driven vertical-external-cavity surface-emitting lasers, *IEEE J. Quantum Electron.* **41**, 1148 (2005).
- [28] M. Marconi, J. Javaloyes, S. Balle, and M. Giudici, How Lasing Localized Structures Evolve Out of Passive Mode Locking, *Phys. Rev. Lett.* **112**, 223901 (2014).
- [29] M. Marconi, J. Javaloyes, P. Camelin, D. C. González, S. Balle, and M. Giudici, Control and generation of localized pulses in passively mode-locked semiconductor lasers, *IEEE J. Sel. Top. Quantum Electron.* **21**, 30 (2015).
- [30] J. Javaloyes, Cavity Light Bullets in Passively Mode-Locked Semiconductor Lasers, *Phys. Rev. Lett.* **116**, 043901 (2016).
- [31] S. V. Gurevich and J. Javaloyes, Spatial instabilities of light bullets in passively-mode-locked lasers, *Phys. Rev. A* **96**, 023821 (2017).
- [32] G. H. M. van Tartwijk and G. P. Agrawal, Laser instabilities: A modern perspective, *Prog. Quantum Electron.* **22**, 43 (1998).
- [33] A. G. Vladimirov, A. S. Pimenov, and D. Rachinskii, Numerical study of dynamical regimes in a monolithic passively mode-locked semiconductor laser, *IEEE J. Quantum Electron.* **45**, 462 (2009).
- [34] A. G. Vladimirov and D. V. Turaev, Model for passive mode locking in semiconductor lasers, *Phys. Rev. A* **72**, 033808 (2005).
- [35] C. Otto, K. Lüdge, A. G. Vladimirov, M. Wolfrum, and E. Schöll, Delay induced dynamics and jitter reduction of passively mode-locked semiconductor laser subject to optical feedback, *New J. Phys.* **14**, 113033 (2012).
- [36] L. C. Jaurigue, O. Nikiforov, E. Schöll, S. Breuer, and K. Lüdge, Dynamics of a passively mode-locked semiconductor laser subject to dual-cavity optical feedback, *Phys. Rev. E* **93**, 022205 (2016).
- [37] J. Wang, A. Maitra, C. G. Poulton, W. Freude, and J. Leuthold, Temporal dynamics of the alpha factor in

- semiconductor optical amplifiers, *J. Lightwave Technol.* **25**, 891 (2007).
- [38] B. Lingnau, W. W. Chow, and K. Lüdge, Amplitude-phase coupling and chirp in quantum-dot lasers: Influence of charge carrier scattering dynamics, *Opt. Express* **22**, 4867 (2014).
- [39] A. S. Pimenov, E. A. Viktorov, S. P. Hegarty, T. Habruseva, G. Huyet, D. Rachinskii, and A. G. Vladimirov, Bistability and hysteresis in an optically injected two-section semiconductor laser, *Phys. Rev. A* **89**, 052903 (2014).
- [40] O. Nikiforov, L. C. Jaurigue, L. Drzewietzki, K. Lüdge, and S. Breuer, Experimental demonstration of change of dynamical properties of a passively mode-locked semiconductor laser subject to dual optical feedback by dual full delay-range tuning, *Opt. Express* **24**, 14301 (2016).
- [41] J. Sieber, K. Engelborghs, T. Luzyanina, G. Samaey, and D. Roose, DDE-BIFTOOL Manual - Bifurcation analysis of delay differential equations, [arXiv:1406.7144](https://arxiv.org/abs/1406.7144).
- [42] C. Otto, B. Globisch, K. Lüdge, E. Schöll, and T. Erneux, Complex dynamics of semiconductor quantum dot lasers subject to delayed optical feedback, *Int. J. Bifurcation Chaos* **22**, 1250246 (2012).
- [43] C. Schelte, J. Javaloyes, and S. V. Gurevich, Dynamics of temporally localized states in passively mode-locked semiconductor lasers, *Phys. Rev. A* **97**, 053820 (2018).
- [44] L. C. Jaurigue, *Passively Mode-Locked Semiconductor Lasers: Dynamics and Stochastic Properties in the Presence of Optical Feedback* (Springer, Cham, Switzerland, 2017), Springer Thesis ed.
- [45] C. G. E. Alfieri, D. Waldburger, R. Nürnberg, M. Golling, L. C. Jaurigue, K. Lüdge, and U. Keller, Modelocking Instabilities for High-Gain Semiconductor Disk Lasers based on Active Submonolayer Quantum Dots, *Phys. Rev. Appl.* **10**, 044015 (2018).
- [46] B. Tromborg, H. E. Lassen, and H. Olesen, Traveling wave analysis of semiconductor lasers: Modulation responses, mode stability and quantum mechanical treatment of noise spectra, *IEEE J. Quantum Electron.* **30**, 939 (1994).
- [47] C. Otto, *Dynamics of Quantum Dot Lasers – Effects of Optical Feedback and External Optical Injection* (Springer, Heidelberg, 2014), Springer Thesis.
- [48] A. G. Vladimirov, D. V. Turaev, and G. Kozyreff, Delay differential equations for mode-locked semiconductor lasers, *Opt. Lett.* **29**, 1221 (2004).